Article

Universal transcriptomic hallmarks of mammalian ageing and mortality

https://doi.org/10.1038/s41586-026-10542-3

Received: 1 July 2024

Accepted: 14 April 2026

Published online: 27 May 2026

Open access

Check for updates

Alexander Tyshkovskiy[1]✉, Daria Kholdina[1,2,3], Maria Davitadze[1,2,3], Adrian Molière[1,4], Alibek Moldakozhayev[1,5,6,7], Yoshiyasu Tongu[8,9], Tomoko Kasahara[9,10], Dmitrii Glubokov[1], Alec Eames[1], Leonid M. Kats[2], Anastasiya Vladimirova[1,11], Kejun Ying[1,12], Hanna Liu[1,13], Bohan Zhang[1], Uma Khasanova[2,3], Mahdi Moqri[1,14], Jeremy M. Van Raamsdonk[5,6,7,15], David E. Harrison[16], Randy Strong[17], Takaaki Abe[9,10,18], Sergey E. Dmitriev[2,3] & Vadim N. Gladyshev[1,19]✉

Ageing and interventions modulate health and mortality[1], yet the underlying molecular mechanisms of this modulation remain unclear. Here we integrate more than 11,000 transcriptomes from more than 25 tissues across 4 mammals (mouse, rat, macaque and human) to develop accurate, interpretable rodent and multi-species biomarkers of chronological age and expected mortality, predicting lifespan-modulating interventions, time to death, chronic diseases and rejuvenation. Ageing-related changes were conserved across species and cell types, revealing universal transcriptomic signatures of mammalian ageing and mortality, including *CDKN1A* and *LGALS3*, whose protein levels were also associated with mortality and multimorbidity in UK Biobank. Mortality-associated features were recapitulated across in vivo and in vitro damage-accumulation models, including inflammation, replicative senescence, metabolic inhibition and γ-irradiation, and were attenuated or reversed by cell immortalization, reprogramming, heterochronic parabiosis and early embryogenesis. Network analysis uncovered a modular architecture of ageing- and mortality-associated hallmarks, encompassing inflammation, interferon signalling, mitochondrial function, chromatin modification and extracellular matrix organization. To quantify ageing of individual cellular components, we developed module-specific clocks, which revealed pathway-specific effects of interventions: chronic diseases primarily accelerated inflammatory-module ageing, whereas caloric restriction and *Klotho* (also known as *Kl*) deficiency targeted mitochondrial and metabolic modules. Transcriptomic and DNA methylation clocks showed correlated age acceleration in human blood, which was strongest for the chromatin-associated module clock, highlighting mechanistic links between molecular ageing modalities. This study reveals conserved signatures and a modular architecture of mortality regulation, providing a framework for quantifying and targeting ageing of cellular subsystems across species and tissues.

Ageing is characterized by systemic damage accumulation, functional decline, and often an exponentially increasing mortality rate[1]. These manifestations can be modulated by genetic, dietary, and pharmacological interventions, ranging from Hutchinson–Gilford progeria syndrome[2] and *Klotho*-knockout (*Klotho*-KO)[3] to caloric restriction[4], rapamycin[5] and dwarf models[6]. Since 2004, the Interventions Testing Program (ITP) has evaluated more than 50 compounds in genetically heterogeneous UM-HET3 mice and identified more than 10 lifespan-extending treatments, including rapamycin[5], acarbose[7], 17-α-oestradiol[7], canagliflozin[8] and others[9]. Although mammalian molecular signatures of ageing[10–14] and lifespan-regulating models[15–18] have been described, a unified analysis of mortality-associated mechanisms shared across ageing, lifespan-shortening models and longevity interventions has been lacking.

High-throughput profiling has enabled epigenetic[19–23], transcriptomic[24–26] and proteomic[27] clocks that estimate chronological age from molecular profiles of tissues or cell types[28,29]. Recently, a pan-mammalian DNA methylation clock revealed conserved age-related epigenetic changes across organs and species[30]. However, biomarkers of mortality and clinical outcomes better reflect cumulative damage burden (molecular age) and improve health prediction[31–33]. Existing DNA methylation mortality clocks are largely restricted to human blood, single-cell applications remain limited, and CpG-based models are often difficult to interpret mechanistically.

A list of affiliations appears at the end of the paper.

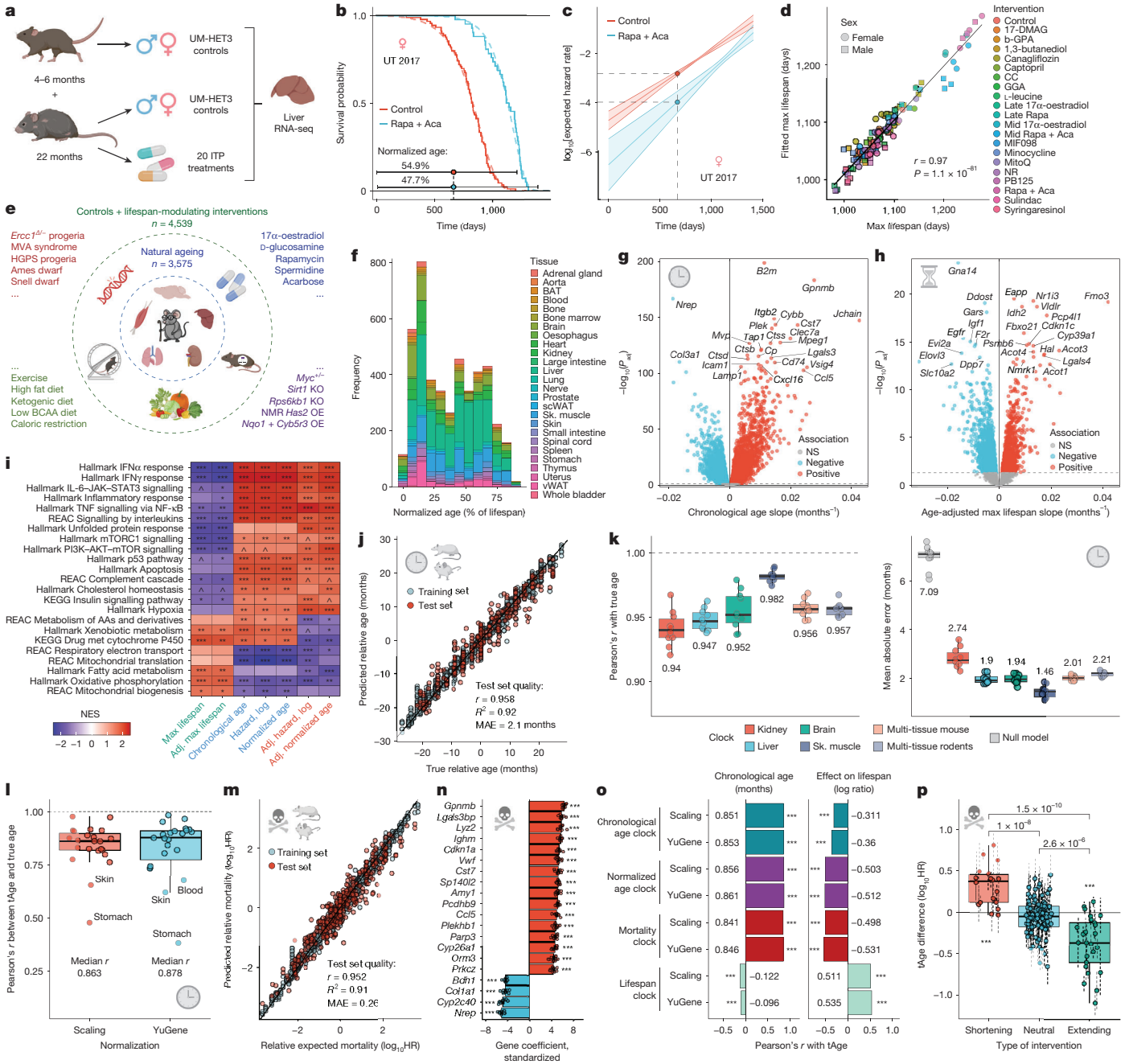

Fig. 1 | See next page for caption.

By contrast, transcriptomic models are more interpretable because genes are functionally annotated, and expression profiling is widely accessible across tissues and species. Single-cell RNA-sequencing (scRNA-seq) and single-nucleus RNA-sequencing (snRNA-seq) approaches further enable quantification of molecular age across cell types and identification of populations that are most responsive to specific interventions. These features make transcriptomic clocks attractive for characterizing universal mortality signatures at both composite and module-level resolution.

Here we generated RNA-sequencing (RNA-seq) data from UM-HET3 mice subjected to 20 ITP interventions and integrated them with published transcriptomes and survival data, encompassing 4,539 rodent samples across 26 tissues. We developed rodent multi-tissue clocks of chronological age and expected mortality and decomposed them into co-regulated modules representing core cellular components. We further incorporated 6,626 primate samples to develop multi-species, multi-tissue transcriptomic clocks. These tools revealed conserved and model-specific mortality hallmarks across tissues, cell types, chronic diseases and damage or rejuvenation interventions. Finally, we provide the Transcriptomic Age Calculator Online (TACO; https://app.gladyshevlab.org/TACO/) web app and the R package tAge to facilitate application of these biomarkers.

Rodent biomarkers of ageing and lifespan

To identify gene expression signatures of lifespan and mortality, we profiled livers from 170 old (22-month-old) genetically heterogeneous UM-HET3 male and female mice exposed to 20 pharmacological ITP interventions or control diets together with 12 young (4- to 6-month-old) controls (Fig. 1a and Supplementary Table 1a). The intervention panel included survival-neutral, detrimental and beneficial compounds, including interventions that robustly extend lifespan in males and/or females

Fig. 1 | Rodent multi-tissue transcriptomic clocks capture molecular changes associated with ageing and mortality. a, Overview of sequenced ITP samples. Schematic created in BioRender; Tyshkovskiy, A. https://BioRender.com/on7cpyb (2026). **b**, Survival of control ITP mice and animals treated with rapamycin (Rapa) and acarbose (Aca), with labelled normalized ages at a given chronological age. UT 2017, University of Texas 2017 cohort. **c**, Gompertz fits of expected all-cause mortality from **b**. Solid lines show model-based point estimates; shaded bands show 95% confidence interval; dots indicate estimated log hazard rate at the specified age. **d**, Maximum lifespan (90th percentile) from raw survival data (*x* axis) or Gompertz fit (*y* axis) across ITP cohorts. Pearson's *r* and *P* value are labelled. 17-DMAG, 17-dimethylaminoethylamino-17-demethoxygeldanamycin hydrochloride; b-GPA, b-guanidinopropionic acid; CC, candesartan cilexetil; GGA, geranylgeranyl acetone; late, late-life; max, maximum; mid, mid-life; MIF098, 3-(3-hydroxybenzyl)-5-methylbenzo[d]oxazol-2(3H)-one; NR, nicotinamide riboside. **e**, Schematic of mouse and rat tissue gene expression samples aggregated for meta-analysis. NMR, naked mole rat; OE, overexpression; BCAA, branched-chain amino acid; HGPS, Hutchinson–Gilford progeria syndrome; KO, knockout; MVA, mosaic variegated aneuploidy. Schematic created in BioRender; Tyshkovskiy, A. https://BioRender.com/l2uq7vs (2026). **f**, Normalized ages and tissues for rodent samples ($n = 4{,}539$). Normalized age is the fraction of expected maximum lifespan (99.9th percentile) for a given age, strain, sex and intervention. BAT, brown adipose tissue; scWAT, subcutaneous white adipose tissue; Sk., skeletal; vWAT, visceral white adipose tissue. **g**, Chronological age gene expression signature from control animals ($n = 3{,}575$); slopes and Benjamini–Hochberg-adjusted *P* values were computed with mixed-effects models. NS, not significant. **h**, Transcriptomic signature of expected maximum lifespan (99.9th percentile) adjusted for age ($n = 4{,}539$); slopes and Benjamini–Hochberg-adjusted *P* values were computed with mixed-effects models. **i**, GSEA of signatures of ageing, maximum lifespan, normalized age and expected mortality, unadjusted and adjusted for age. Benjamini–Hochberg-adjusted *P* values were computed using GSEA permutation tests. Full results are in Supplementary Table 3b. AAs, amino acids; Adj., adjusted; KEGG, Kyoto Encyclopedia of Genes and Genomes; met, metabolism; NES, normalized enrichment score; REAC, Reactome. **j**, Performance of elastic net rodent multi-tissue transcriptomic clock of relative chronological age (scaling normalization) on training ($n = 3{,}217$) and test ($n = 358$) sets. Pearson's *r*, R^2 and MAE on test set are provided. **k**, Accuracy of organ-specific and multi-tissue relative chronological age clocks across ten randomly selected test sets. Median metrics are labelled; null-model MAE in grey. **l**, Leave-one-tissue-out performance of the elastic net multi-tissue chronological age clock ($n = 23$ tissues). Median Pearson's *r* across tissues is labelled. **m**, Performance of elastic net rodent multi-tissue transcriptomic clock of relative expected mortality (YuGene-based) on training ($n = 4{,}038$) and test ($n = 449$) sets. HR, hazard ratio. **n**, Top 20 genes with largest absolute coefficients in the elastic net mortality clock (YuGene-based). Data are mean standardized coefficients ± s.e.m. $n = 10$ randomly selected training sets; significance was tested with one-sample *t*-test. **o**, Accuracy of elastic net clocks in predicting chronological age (left) and intervention lifespan effects (right) in independent datasets (Pearson's *r*). Lifespan effect was computed for each dataset, sex and intervention as the log-ratio of maximum lifespan for treated versus control animals. Median *r* is labelled. $^{\wedge}P < 0.1$, $^{*}P < 0.05$, $^{**}P < 0.01$, $^{***}P < 0.001$. **p**, Mean mortality tAge differences between treated and control samples across lifespan-shortening ($n = 18$), neutral ($n = 91$) and lifespan-extending ($n = 25$) interventions, evaluated separately for each dataset and sex using elastic net rodent multi-tissue mortality clock. Deviation from zero and between-group differences were tested with mixed-effects models; Benjamini–Hochberg-adjusted *P* values are labelled. Data are ANOVA coefficients ± standard error (s.e.). In box plots, the centre line is the median, box edges delineate interquartile range (IQR) and whiskers extend to ±1.5× IQR. All tests were two-sided where applicable. *P* values were Benjamini–Hochberg-adjusted unless noted; asterisks denote Benjamini–Hochberg-adjusted *P* values: $^{\wedge}P_{adj} < 0.1$; $^{*}P_{adj} < 0.05$; $^{**}P_{adj} < 0.01$; $^{***}P_{adj} < 0.001$. Icons in **g**,**h**,**j**–**n**,**p** created in BioRender; Tyshkovskiy, A. https://BioRender.com/hqvg5ka (2026).

(rapamycin, canagliflozin, captopril, 17-α-oestradiol and rapamycin plus acarbose). This design enabled joint analysis of ageing- and lifespan-regulating molecular changes within a unified mortality framework.

To estimate expected all-cause mortality for each animal, we fitted Gompertz models to ITP survival data for each cohort, sex, site and intervention (Fig. 1b), and aggregated cohort-level fits by sex and intervention into Gompertz meta-models (Extended Data Fig. 1a,b). For each sequenced mouse, we then calculated expected log hazard rate (Fig. 1c) as the mean prediction from the cohort-specific fit and its corresponding meta-model given age and experimental group (Methods). Model-simulated 90th percentile lifespans closely matched empirical estimates from survival curves (Fig. 1d), supporting the use of Gompertz fits to capture intervention effects on longevity. We also computed normalized age as chronological age divided by expected maximum (99.9th percentile) lifespan (Extended Data Table 1), yielding two composite metrics—expected mortality and normalized age—that integrate chronological ageing with intervention-induced lifespan modulation.

Principal component analysis (PCA) of liver transcriptomes separated samples primarily by sex (Extended Data Fig. 1c). Regression across cohorts identified 700–1,457 genes (adjusted *P* value (P_{adj}) < 0.05) associated with chronological age, normalized age, expected mortality and maximum lifespan after adjustment for sex and site (Supplementary Table 2a–g). Comparison of regression slopes across traits revealed positive correlation of chronological ageing signature with age-adjusted signatures of normalized age and expected mortality and its negative correlation with the lifespan signature (Extended Data Fig. 1d), suggesting that age-associated expression changes largely track health deterioration rather than neutral drift. These signatures were highly concordant between sexes (Extended Data Fig. 1e) despite the sex-specific lifespan-extending effects of certain interventions, such as 17-α-oestradiol and canagliflozin[7–9].

Among the top genes that were positively associated with maximum lifespan and negatively associated with chronological age and expected mortality, we identified *Gpx1* (Extended Data Fig. 1f,g), encoding glutathione peroxidase 1, whose overexpression ameliorates murine age-related renal pathology[34]. Other oxidative stress and metabolic genes, including several cytochrome P450 and fatty acid metabolism enzymes, showed similar trends.

Gene set enrichment analysis (GSEA) identified pathways that were positively associated with lifespan and negatively associated with ageing and mortality (Supplementary Table 3a), including oxidative phosphorylation, mitochondrial biogenesis, xenobiotic metabolism and fatty acid metabolism, whereas interferon signalling and haemostasis showed the opposite pattern (Extended Data Fig. 1h). Pathway-level enrichment scores mirrored gene-level relationships across traits (Extended Data Fig. 1i).

To generalize beyond ITP, we assembled a rodent gene expression meta-dataset comprising 3,575 mouse and rat samples across 26 tissues, spanning a broad age range (4–943 days) and multiple strains (Extended Data Fig. 1j), together with 964 additional samples from animals subjected to diverse pharmacological, genetic, dietary, and environmental interventions with extending, shortening, or neutral effects on lifespan (Fig. 1e). In total, this yielded 4,539 rodent transcriptomes across 96 data sources and 79 interventions (Supplementary Table 1b).

Using published survival data, we again fitted cohort-specific and aggregated Gompertz models by strain, sex and intervention to compute expected log hazard rate, normalized age and maximum lifespan for each sample (Fig. 1f and Extended Data Fig. 1k). Consistently, model-simulated 90th percentile lifespans closely tracked empirical estimates (Extended Data Fig. 1l). Expected mortality increased with age and was modulated by genetic background, progeroid models, high-fat diets and lifespan-extending treatments (Extended Data Fig. 1m).

For cross-study multi-tissue signatures, we computed relative expression by centring each sample to the median profile of a randomly selected matched control group within the same dataset, tissue and sex (Methods). Linear mixed-effects models revealed 9,059–9,167 genes

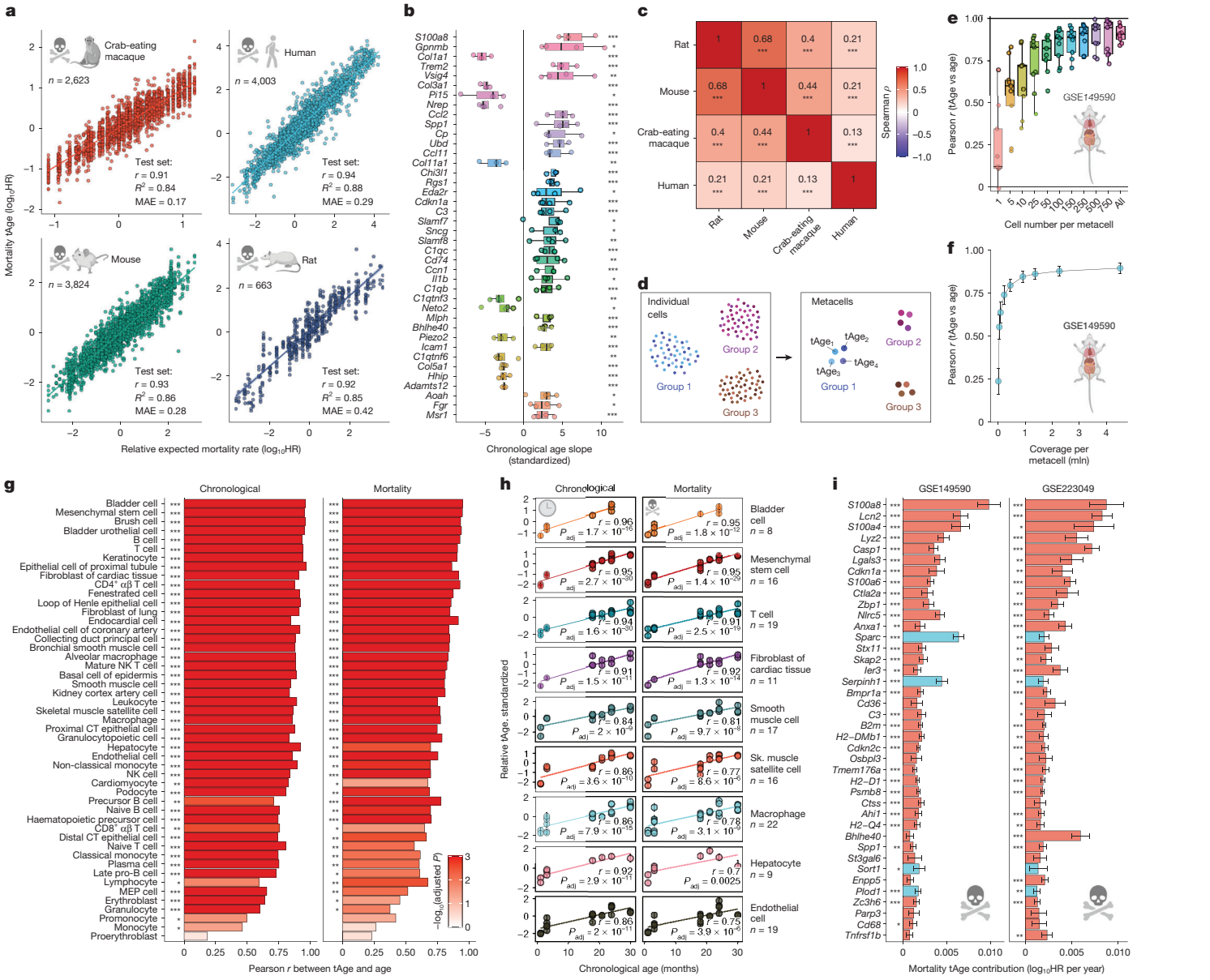

Fig. 2 | Transcriptomic biomarkers of ageing and mortality are conserved across mammalian species and cell types. a, LOFO performance of elastic net multi-species multi-tissue clock of relative expected mortality (YuGene-based). Clocks were evaluated by tenfold nested cross-validation in mouse ($n = 3,824$), rat ($n = 663$), crab-eating macaque ($n = 2,623$) and human ($n = 4,003$); test predictions shown. Pearson's r, R^2 and MAE across all test predictions are labelled. **b**, Top 40 genes consistently associated with age ($P_{adj} < 0.05$) across tissues and species, tested with mixed-effects models. Each dot is the standardized age slope of expression for one species. For each gene, n equals the number of shown dots ($n = 3$ or $n = 4$). **c**, Pairwise Spearman correlations of gene expression age slopes across species, computed using the union of the top 1,000 age-associated genes (lowest mixed-effects-model P values) per pair. **d**, Metacell-based scRNA-seq analysis of tAge. Transcriptomic clocks are applied to pseudobulk profiles pooled from randomly selected cells of the same type and condition. **e**, Accuracy of age prediction by the BR mouse multi-tissue chronological clock versus metacell size across Tabula Muris Senis tissues ($n = 9$ tissues). Each dot represents Pearson's r for one tissue. **f**, Accuracy of age prediction by BR chronological clock versus mean gene coverage per metacell ($n = 9$ tissues). mln, million reads. Data are mean Pearson's r across tissues ± s.e.m. **g**, Pearson correlations between chronological age and tAge estimated with BR mouse chronological (left) and mortality (right) clocks for individual cell types; significance was tested with mixed-effects models. CT, convoluted tubule; MEP, megakaryocyte–erythroid progenitors; NK, natural killer. **h**, tAge dynamics in representative cell types estimated with BR chronological (left) and mortality (right) clocks. tAges were standardized within each cell type and clock. Pearson's r and Benjamini–Hochberg-adjusted P values are labelled. The number of animals (n) is provided next to the cell-type label. Solid lines show linear regression fits. Data are tAge point estimates ± s.d. **i**, Top 40 genes contributing to mortality-associated transcriptomic shifts across cell types during ageing in two independent mouse datasets (GSE149590: $n = 762$ samples across 49 cell types; GSE223049: $n = 164$ samples across 22 cell types). Contributions were calculated as (age slope or log fold change (FC) across cell types) × (coefficient of elastic net mouse multi-tissue mortality clock). Only genes present in both datasets are shown. Data are slope point estimates ± s.e. In box plots, the centre line is the median, box edges delineate IQR and whiskers extend to ±1.5× IQR. All tests were two-sided where applicable. P values were Benjamini–Hochberg-adjusted unless noted; asterisks denote Benjamini–Hochberg-adjusted P values: $^*P_{adj} < 0.05$; $^{**}P_{adj} < 0.01$; $^{***}P_{adj} < 0.001$. Icons in **a**,**e**,**f**,**h**,**i** created in BioRender; Tyshkovskiy, A. (2026) https://BioRender.com/hqvg5ka (2026).

associated with chronological age, normalized age and expected mortality ($P_{adj} < 0.05$), and 3,098–4,439 genes associated with maximum lifespan and mortality-related traits after age adjustment (Fig. 1g,h, Extended Data Fig. 1n and Supplementary Table 2h–n), indicating systemic regulation of longevity and mortality at the molecular level.

Notable genes negatively associated with lifespan included *Igf1*, a canonical longevity regulator within and across species[13,35], and *Ddost*, which is involved in advanced glycation end product processing and linked to poorer cancer survival[36], whereas pro-longevity genes included *Fmo3*, an mTOR and inflammation inhibitor, and *Nmrk1*, which is involved in NAD^+ biosynthesis. *Igf1* expression tended to decline with age, whereas *Fmo3* expression increased (Extended Data Fig. 1o), indicating that ageing-related changes include both detrimental and compensatory components.

Consistent with results from ITP, signatures of chronological age overlapped with age-adjusted mortality signatures and opposed lifespan signatures at gene and pathway levels (Extended Data Fig. 1p–r). Interferon, interleukin and p53 signalling, complement and coagulation, and other inflammatory and stress-response programmes were negatively associated with lifespan and positively associated with ageing and mortality, whereas oxidative phosphorylation and mitochondrial translation showed the opposite pattern (Fig. 1i and Supplementary Table 3b). Fatty acid and xenobiotic metabolism were also negatively associated with mortality, supporting roles in longevity regulation[15,17,37] and accumulated damage clearance[1]. Together, these analyses define conserved rodent transcriptomic signatures of ageing, mortality and lifespan across a large multi-tissue meta-dataset.

Ageing and mortality multi-tissue clocks

To develop quantitative multi-tissue transcriptomic biomarkers of ageing and mortality, we used the aggregated rodent dataset to train models predicting chronological age, normalized age and expected hazard. For the chronological clock, we trained an elastic net model on 3,575 control mouse and rat bulk transcriptomes across 26 tissues (Extended Data Fig. 1j). It accurately predicted absolute chronological age (divided by species maximum recorded lifespan) in held-out samples ($R^2 = 0.88$; Pearson's $r = 0.94$; Extended Data Fig. 2a), yielding similar performance across two normalization strategies (scaling and YuGene; Methods) and robust results across random train–test splits (Extended Data Fig. 2b).

To further improve performance by reducing batch effects, we constructed 'relative' clocks by centring each transcriptome sample to a randomly chosen matched control reference group within the same dataset and tissue and predicting the corresponding age difference (Fig. 1j). This increased the accuracy of the rodent multi-tissue clock (median $R^2 = 0.92$; median $r = 0.96$, Extended Data Fig. 2b and Supplementary Table 4a) and was robust to reference group selection (Extended Data Fig. 2c), reaching performance comparable to epigenetic clocks[19,21,22,30]. To estimate transcriptomic age (tAge) uncertainty, which is particularly useful for small sample sizes, we also trained Bayesian ridge (BR) versions of clocks, which achieved similar accuracy (Extended Data Fig. 2b).

Tissue-specific chronological clocks (kidney, liver, brain and skeletal muscle) and a mouse-specific multi-tissue model performed comparably to the rodent clock (median $r = 0.94–0.982$; Fig. 1k and Supplementary Table 4a), indicating that integrating tissues does not substantially reduce performance. Alternative machine learning models (support-vector machines (SVM), light gradient-boosting machine (LightGBM), random forest and *k*-nearest neighbours (KNN)) did not outperform the elastic net model (Extended Data Fig. 2d).

To assess model generalizability across tissues and datasets, we performed leave-one-tissue-out (LOTO) and leave-one-dataset-out (LODO) tests. In LOTO analyses, relative multi-tissue chronological clocks captured age dynamics in all held-out tissues (median $r = 0.863–0.878$; Fig. 1l and Extended Data Fig. 2e), indicating that systemic ageing-associated signatures are shared across organs. In LODO analyses, relative clocks outperformed absolute clocks in independent datasets ($r = 0.85$, mean absolute error (MAE) = 4 months; Extended Data Fig. 2f,g), supporting the effectiveness of within-dataset centring to mitigate batch effects. Thus, we focused on relative clocks throughout the study.

To develop an integrated model capturing ageing and intervention lifespan-modulating effects, we utilized the full meta-dataset to train rodent multi-tissue clocks of normalized age and expected mortality (Fig. 1m and Extended Data Fig. 2h). Relative models again outperformed absolute ones (median $r = 0.94–0.95$), were robust to reference group selection (Extended Data Fig. 2i), and showed similar performance for elastic net and BR (Supplementary Table 4a). In LODO tests, these clocks retained predictive power in independent datasets ($r = 0.81–0.85$; Extended Data Fig. 2j,k).

Clock coefficients were positively correlated across chronological age, normalized age and mortality models (Extended Data Fig. 2l). Among the top positive features shared by chronological and mortality clocks were *Gpnmb*, *Cst7* and *Cdkn1a* (Fig. 1n, Extended Data Fig. 2m and Supplementary Table 5a), encoding GPNMB (an inflammation-associated glycoprotein[38]), CST7 (a lysosomal cathepsin inhibitor implicated in neurodegeneration[39]) and CDKN1A/p21 (a p53 pathway cell cycle inhibitor[40]). By contrast, genes with top negative mortality coefficients included *Nrep*, *Col1a1* and *Col3a1*, which are linked to differentiation and wound healing, presumably reflecting the loss of regenerative capacity during ageing and in short-lived animals[41]. In line with the clock coefficients, expression of *Cst7* and *Cdkn1a* increased with ageing and age-adjusted mortality, whereas expression of *Nrep*, *Col1a1* and *Col3a1* decreased as ageing and age-adjusted mortality increased (Extended Data Fig. 1o).

We next tested whether clocks captured both chronological ageing and lifespan-modulating effects by correlating their predictions with age and intervention-associated changes in expected maximum lifespan in independent datasets. As a benchmark, we trained a 'lifespan clock' that directly predicts maximum-lifespan differences from expression changes (Extended Data Fig. 3a). Adding chronological age as a feature did not significantly improve its performance (Extended Data Fig. 3b), indicating that age was already sufficiently encoded in expression profiles. Predictions of chronological clocks exhibited high correlation with age but low correlation with intervention-induced lifespan changes, whereas the lifespan clock showed the opposite pattern (Fig. 1o and Extended Data Fig. 3c). By contrast, normalized-age and mortality clocks tracked both age and lifespan effects, with consistent performance across tissues (Extended Data Fig. 3d).

When interventions were stratified into lifespan-shortening and lifespan-extending models, the chronological clock detected detrimental interventions (higher tAge compared to age-matched controls) but did not robustly capture lifespan extension (Extended Data Fig. 3e), consistent with reports that longevity interventions often do not strongly reverse age-related transcriptomic signatures[13,18]. By contrast, normalized-age and especially mortality clocks distinguished both short-lived and long-lived models ($P_{adj} < 6 \times 10^{-4}$ and $P_{adj} < 3 \times 10^{-6}$, respectively), predicting higher tAge for detrimental and lower tAge for longevity interventions (Fig. 1p and Extended Data Fig. 3e). Notably, the mortality clock discriminated lifespan-modulating models better than the dedicated lifespan clock, suggesting that integrating ageing and intervention information improves the overall performance of molecular health biomarkers.

Conserved cross-species ageing biomarkers

To examine whether multi-tissue signatures of ageing and mortality are conserved across rodents and primates, we expanded the meta-dataset

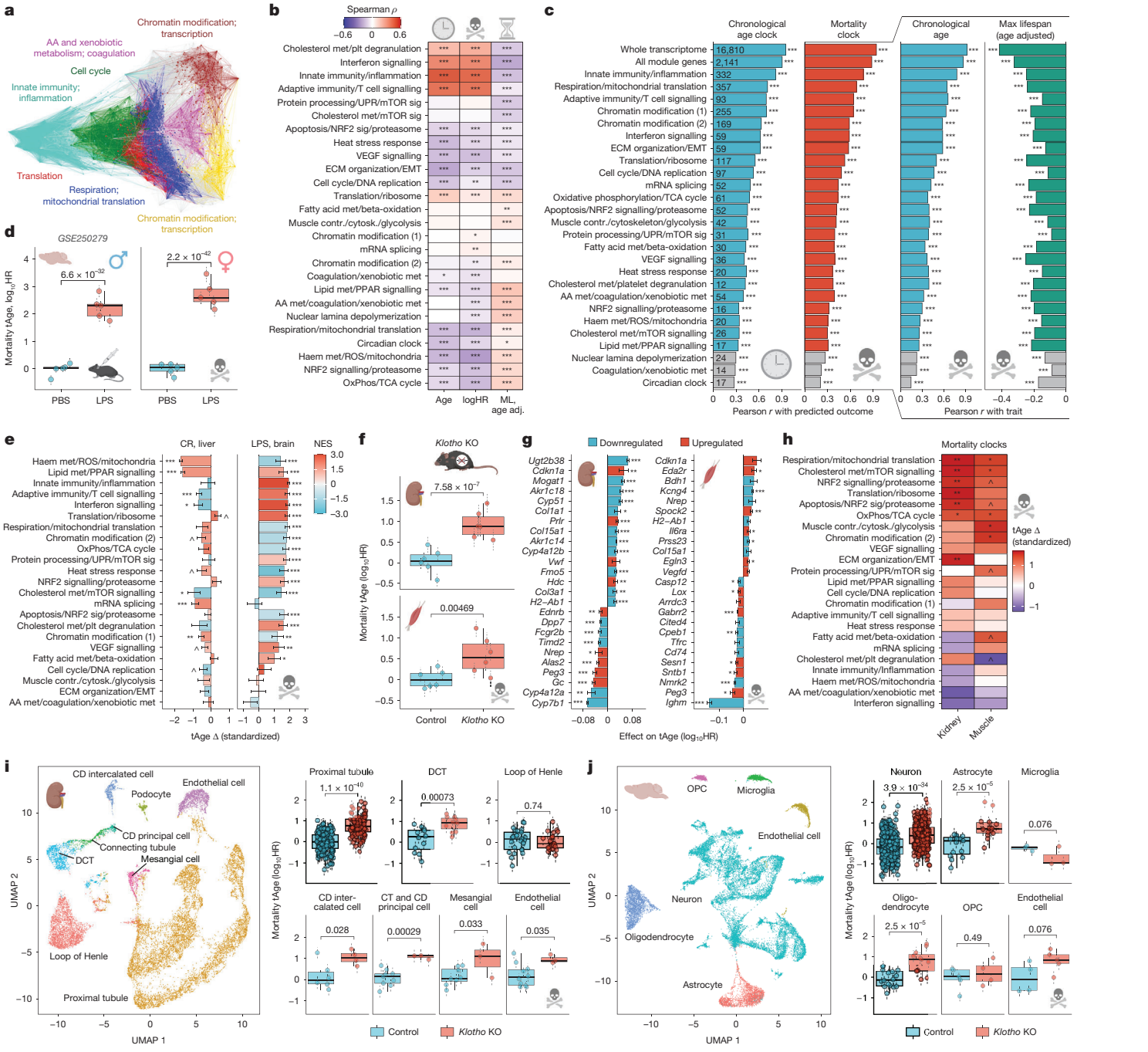

Fig. 3 | See next page for caption.

with 2,623 crab-eating macaque samples from more than 30 tissues and 4,003 human samples from brain, skeletal muscle, skin and blood (Supplementary Table 1c). For each sample, we computed chronological age (scaled to species maximum lifespan), normalized age and expected mortality using published survival data.

Utilizing this meta-dataset, we then trained unified multi-species, multi-tissue ('universal') relative clocks of chronological age, normalized age and expected mortality. These models performed well across all four species (Fig. 2a, Extended Data Fig. 3f and Supplementary Table 4a), achieving within-species Pearson's $r \geq 0.94$ (chronological clocks) and $r \geq 0.91$ (mortality clocks) in leave-one-fold-out (LOFO) validation. Across all test samples, chronological tAge correlated with age at $r = 0.952$, comparable to a pan-mammalian DNA methylation clock[30] ($r = 0.953$). In leave-one-species-out (LOSO) analyses, the chronological clock captured ageing trajectories in unseen species ($0.66 \leq r \leq 0.84$; Extended Data Fig. 3g), indicating generalizability of core transcriptomic features of ageing across mammals.

Cross-species comparisons revealed conserved gene- and pathway-level ageing signatures. Consistent upregulated genes across rodents and primates included *Gpnmb*, *Vsig4*, *Cdkn1a* and *Eda2r*, whereas conserved downregulated markers included *Nrep*, *Col1a1* and *Col3a1* (Fig. 2b and Supplementary Table 2o–r). Species-specific ageing slopes were positively correlated, both globally and within individual tissues (Fig. 2c and Extended Data Fig. 3h,i). Concordant functional changes across species included upregulation of interferon, TNF and p53 signalling, hypoxia and complement/coagulation, together with downregulation of DNA repair, mitochondrial translation, oxidative phosphorylation and collagen formation (Extended Data Fig. 3j and Supplementary Table 3c). Together, these results support a conserved transcriptomic architecture of mammalian ageing across tissues and species.

Fig. 3 | Co-regulated gene expression modules define fundamental molecular hallmarks of ageing and longevity. a, Gene co-expression network (spectral embedding) with selected coloured modules identified by WGCNA; representative enriched pathways are labelled. AA, amino acid. **b**, Spearman correlations between the first principal component of each module and chronological age (left), expected mortality (logHR; middle) or age-adjusted expected maximum lifespan (ML; right). Contr., contraction; cytosk., cytoskeleton; OxPhos, oxidative phosphorylation; plt, platelet; sig, signalling; TCA, tricarboxylic acid. **c**, Performance of elastic net rodent multi-tissue clocks trained on genes from individual modules, all modules combined or the whole transcriptome. Left, LOFO performance (Pearson's *r*) of chronological (blue) and mortality (red) clocks. Right, Pearson's *r* between mortality tAge and chronological age (blue) or age-adjusted expected maximum lifespan (green). Feature set sizes are labelled; clocks with mean $r < 0.3$ are shown in grey and excluded. **d**, Mortality tAge of brains from 5- to 6-month-old male (left) and female (right) C57BL/6J mice injected with PBS or LPS ($n = 5$ animals per group), estimated with the BR rodent multi-tissue mortality clock. Benjamini–Hochberg-adjusted *P* values from mixed-effects models are labelled. Data are tAge point estimates ± s.d. **e**, Standardized mortality tAge differences induced by caloric restriction (CR) in liver (left; $n = 8$ caloric restriction models) and LPS in brain (right; $n = 5$ animals per group), estimated with module-specific mortality clocks. Effects of caloric restriction were aggregated across datasets and conditions, and tested using mixed-effects models; LPS effects were tested with ANOVA. Colour indicates module-level expression shifts, quantified by NES through GSEA. Data are point estimates ± s.e. UPR, unfolded protein response **f**, Mortality tAge of kidneys (top) and muscles (bottom) in *Klotho*-KO and control C57BL/6J mice ($n = 6$ mice per group), estimated with the BR rodent multi-tissue mortality clock trained excluding *Klotho*. Benjamini–Hochberg-adjusted *P* values from mixed-effects models are labelled. Data are tAge point estimates ± s.d. **g**, Top 25 genes contributing to pro- or anti-mortality transcriptomic changes in *Klotho*-KO kidneys (left) and muscles (right) ($n = 6$ mice per group), based on the elastic net rodent mortality clock trained excluding *Klotho*. Values are logFC × clock coefficient; significance was tested with limma. Data are point estimates of gene contribution ± s.e. **h**, Standardized mortality tAge differences between *Klotho*-KO and control mice across module-specific mortality clocks; significance was tested with ANOVA. **i**,**j**, UMAP (left) and mortality tAge differences between metacells of control and *Klotho*-KO mice across cell types (right) in kidney (**i**) and brain (**j**), estimated with BR rodent mortality clocks trained excluding *Klotho*. Benjamini–Hochberg-adjusted *P* values from mixed-effects models are indicated. Data are tAge point estimates ± s.d. In box plots, the centre line is the median, box edges delineate IQR and whiskers extend to ±1.5× IQR. All tests were two-sided where applicable. *P* values were Benjamini–Hochberg-adjusted unless noted; asterisks denote Benjamini–Hochberg-adjusted *P* values: $^{\wedge}P_{adj} < 0.1$; $^{*}P_{adj} < 0.05$; $^{**}P_{adj} < 0.01$; $^{***}P_{adj} < 0.001$. CD, collecting duct; CT, connecting tubule; DCT, distal convoluted tubule; OPC, oligodendrocyte precursor cells. Icons in **b**–**j** created in BioRender; Tyshkovskiy, A. https://BioRender.com/hqvg5ka (2026).

Molecular ageing of individual cell types

To examine whether organ-level ageing and mortality signatures are recapitulated within individual cell types, we analysed the Tabula Muris Senis droplet scRNA-seq dataset, which covers multiple tissues from C57Bl/6J mice across different ages. To increase sample coverage, we utilized a metacell approach, pooling counts from randomly selected cells of the same tissue and organism (Fig. 2d). We first validated this strategy by aggregating all available cells per tissue and animal and applying the mouse multi-tissue chronological clock. The clock captured age dynamics across organs with high accuracy (median $r = 0.92$; Extended Data Fig. 3k,l). Varying metacell size revealed a saturating relationship between coverage and clock performance: median $r = 0.90$ across tissues (95% of maximum) at around 100 cells (approximately 1M reads) per metacell, and median $r = 0.84$ (around 89% of maximum) at 25 cells (200K–250K reads) (Fig. 2e,f).

We then applied the metacell procedure and multi-tissue clocks separately to each cell type. Notably, 48 out of 49 (98%) and 46 out of 49 (94%) cell types showed significant positive correlations between mouse chronological age and tAge predicted by chronological and mortality clocks, respectively (Fig. 2g,h and Extended Data Fig. 4a). This was independently supported using transcriptomes of cell types sorted by fluorescence-activated cell sorting (FACS) from young (2-month-old) and old (22- to 24-month-old) C57BL/6 female mice, where both clocks detected significant tAge differences for all cell types with at least 3 samples per group (Extended Data Fig. 4b,c). Notably, stem cell populations (mesenchymal and haematopoietic stem cells) also exhibited substantial pro-mortality expression shifts, indicating that ageing-associated changes extend beyond differentiated lineages.

Accordingly, gene-level contributions to increased tAge during ageing were positively correlated across cell types (Extended Data Fig. 4d). Top shared pro-mortality changes included upregulation of senescence-, inflammation- and apoptosis-associated genes, such as *Cdkn1a*, *Lgals3*, *Casp1*, *S100a8* and *S100a4*, and downregulation of *Sparc*, which encodes a regulator of extracellular matrix (ECM) synthesis, differentiation and wound healing (Fig. 2i). Together, these data indicate that ageing is accompanied by conserved transcriptomic hallmarks of damage accumulation across tissues and cell types, despite their diverse identities and functions.

Module clocks track mortality hallmarks

To identify co-regulated transcriptomic components of ageing and longevity that could serve as pathway-specific quantitative biomarkers, we applied weighted gene co-expression network analysis (WGCNA) to the rodent meta-dataset of relative expression centred within each dataset, tissue and sex (Methods). This revealed 28 robust modules (Fig. 3a), each comprising 30–630 genes with coordinated expression changes during ageing and across interventions. Modules derived independently in males and females significantly overlapped (Extended Data Fig. 5a), indicating robustness across sexes. After filtering (Extended Data Fig. 5b), modules showed largely distinct pathway enrichments with minimal overlap (Extended Data Fig. 5c), including modules enriched for inflammatory/innate immune response, mitochondrial translation/electron transport and ECM organization/epithelial-to-mesenchymal transition (EMT) (Supplementary Table 6a,b).

To assess the biological coherence of the modules, we examined partial correlations between their first principal components after adjusting for chronological age (Extended Data Fig. 5d,e). Functionally related modules clustered together—for example, immune modules (inflammation, interferon and T cell signalling) grouped separately from metabolism-related modules. Consistent with gene- and pathway-level results (Fig. 1i), immune modules were positively associated with age and mortality and negatively associated with expected maximum lifespan, whereas mitochondrial translation, oxidative phosphorylation and lipid metabolism modules showed the opposite pattern (Fig. 3b and Extended Data Fig. 5d,e). Most modules displayed opposing associations with ageing versus lifespan; however, heat stress response, translation and ECM/EMT modules showed co-directional correlations with both metrics, suggesting adaptive or compensatory responses. Some modules (for example, protein processing in the endoplasmic reticulum and mTOR signalling) were associated with longevity but not age, indicating lifespan regulation that is partly independent of chronological ageing.

To develop a compact panel of biomarkers based on these transcriptomic network components, we trained multi-tissue clocks of chronological age and expected mortality for each module (Fig. 3c and Extended Data Table 1). A global model trained on all module genes (2,141 genes) performed comparably to full-transcriptome clocks ($r = 0.88$–0.90 in LOFO validation), indicating that these modules

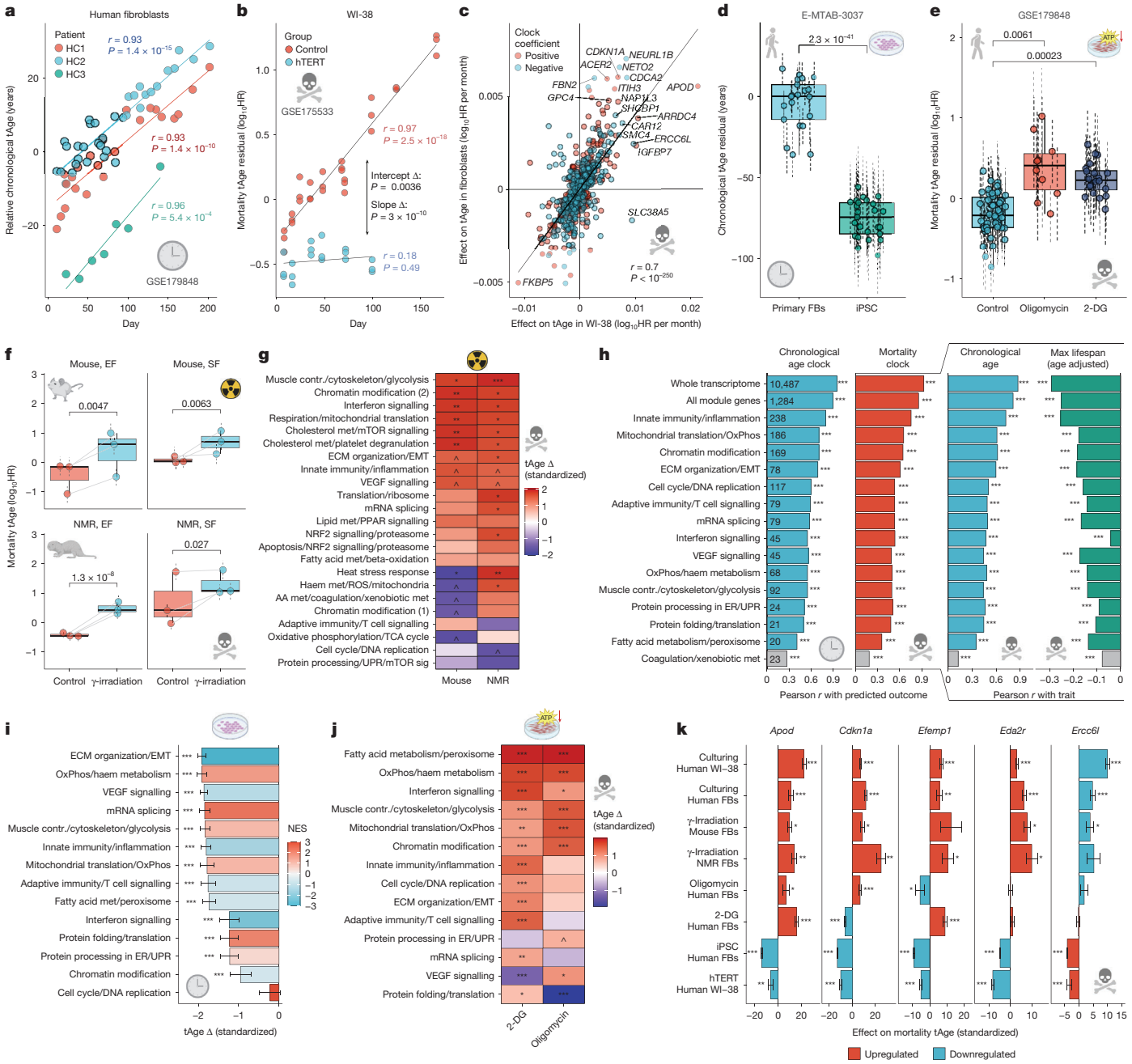

Fig. 4 | See next page for caption.

together capture most mortality-associated variation. Individual module clocks predicted their target variables with moderate accuracy (median $r = 0.41–0.44$; Supplementary Table 4b). After excluding poorly performing modules (mean $r < 0.3$), we retained 23 functionally annotated module-specific clocks of chronological age and mortality (Fig. 3c, left and Supplementary Table 5b). All mortality clocks correlated positively with chronological age and negatively with expected maximum lifespan in test samples (Fig. 3c, right), consistent with the composite nature of the mortality metric. Inter-module relationships were preserved at the tAge level—for example, predictions of immunity-related clocks clustered together (Extended Data Fig. 5f,g).

We next validated module-specific clocks in an established in vivo model of acute inflammatory stress, applying them to brain gene expression data from 5- to 6-month-old C57BL/6J mice injected with lipopolysaccharide (LPS) or phosphate-buffered saline (PBS). LPS increased tAge in both sexes according to composite chronological and mortality clocks (Fig. 3d and Extended Data Fig. 5h) and across most module clocks (Fig. 3e and Extended Data Fig. 5i,j), with the strongest pro-mortality shifts in immune modules (inflammation, interferon signalling and adaptive immune response), consistent with LPS-induced neuroinflammation[42]. Enrichment analysis of differentially expressed genes confirmed robust induction of inflammatory pathways (Fig. 3e and Supplementary Table 7a).

Conversely, liver samples from calorically restricted mice exhibited reduced tAge relative to age-matched controls across many mortality module clocks (Fig. 3e and Extended Data Fig. 6a,b), with the strongest effects in metabolism-related modules (haem metabolism/reactive oxygen species (ROS) pathways, lipid metabolism/PPAR signalling and cholesterol metabolism/mTOR signalling). Consistently, caloric restriction induced broad upregulation of genes involved in cellular respiration, oxidative phosphorylation and lipid, haem, fatty acid and amino acid metabolism (Extended Data Fig. 6c and

Fig. 4 | Tissue-based transcriptomic clocks detect cellular ageing and damage accumulation in vitro. a, Chronological tAge dynamics during culturing of human primary fibroblasts ($n = 65$) estimated with the elastic net universal chronological clock. Pearson's r and P values are labelled for each patient. **b**, Mortality tAge dynamics during culturing of control ($n = 30$) and hTERT-transduced ($n = 18$) WI-38 cells estimated with the elastic net universal mortality clock. Batch-adjusted tAge residuals are plotted. Pearson's r and P values are shown for each condition. Intercept and slope differences were tested with linear models (P values labelled in black). **c**, Concordance of gene-level mortality-associated expression changes (slope × clock coefficient) between cultured primary fibroblasts and control WI-38 cells based on the elastic net universal mortality clock. Union of the top 2,000 differentially expressed genes (lowest limma model P values) significant in both models ($P_{adj} < 0.05$) is shown. Clock coefficient sign is colour-coded. **d**, Chronological tAge residuals of primary fibroblasts (FBs) ($n = 24$) and matched induced pluripotent stem cells ($n = 25$), estimated with the BR universal chronological clock. P value from mixed-effects model adjusted for donor ID is shown. Data are tAge residuals ± s.d. **e**, Mortality tAge residuals of control ($n = 46$), oligomycin-treated ($n = 10$) and 2-DG-treated ($n = 20$) human primary fibroblasts (cultured ≥40 days), estimated with the BR universal mortality clock. Benjamini–Hochberg-adjusted P values from mixed-effects models adjusted for donor and culture time are shown. Data are tAge residuals ± s.d. **f**, Mortality tAge of mouse and naked mole rat skin fibroblasts (SF) and embryonic fibroblasts (EF) under control and γ-irradiation conditions ($n = 3$ per group), estimated with the BR rodent multi-tissue mortality clock. Benjamini–Hochberg-adjusted P values from mixed-effects models adjusted for cell line ID are labelled. Data are tAge point estimates ± s.d. **g**, Standardized mortality tAge differences between irradiated and control mouse (left) and naked mole rat (right) fibroblasts estimated with module-specific rodent mortality clocks; embryonic and skin fibroblasts were pooled. Differences were tested with ANOVA adjusted for cell line ID. **h**, Accuracy of elastic net multi-species multi-tissue clocks trained on genes from individual modules, all modules combined or the whole transcriptome. Left, LOFO performance (Pearson's r) of chronological (blue) and mortality (red) clocks. Right, Pearson's r between mortality tAge and chronological age (blue) or age-adjusted expected maximum lifespan (green). Feature set sizes are labelled; clocks with mean $r < 0.3$ are shown in grey and excluded. ER, endoplasmic reticulum. **i**, Standardized chronological tAge changes induced by human fibroblast reprogramming ($n = 49$), assessed with module-specific universal chronological clocks. Differences were tested with ANOVA adjusted for donor ID. Colour indicates module-level expression shifts (NES computed through GSEA). Data are point estimates ± s.e. **j**, Standardized mortality tAge changes after oligomycin or 2-DG treatment assessed with module-specific universal mortality clocks. Significance was tested with ANOVA adjusted for patient ID and culturing time. **k**, Top 5 genes contributing to mortality tAge changes across cellular models (standardized logFC or slope × clock coefficient), according to the elastic net universal mortality clock. Genes were ranked based on mixed-effects model estimates. Data are point estimates of gene contributions ± s.e. In box plots, the centre line is the median, box edges delineate IQR and whiskers extend to ±1.5× IQR. All tests were two-sided where applicable. P values were Benjamini–Hochberg-adjusted unless noted; asterisks denote Benjamini–Hochberg-adjusted P values. $^{\wedge}P_{adj} < 0.1$; $^{*}P_{adj} < 0.05$; $^{**}P_{adj} < 0.01$; $^{***}P_{adj} < 0.001$. Icons in **a**–**k** created in BioRender; Tyshkovskiy, A. https://BioRender.com/hqvg5ka (2026); and Tyshkovskiy, A. https://BioRender.com/vb612zl (2026).

Supplementary Table 7a), aligning with its metabolic remodelling and lifespan-extending effects[4,43]. Together, these results illustrate that molecular age can be modulated through distinct biological pathways and that module-specific clocks provide an interpretable framework to quantify the pathway-level effects of detrimental or health-promoting interventions.

Pro-mortality effects of *Klotho* knockout

To further validate our biomarkers and characterize mortality-associated mechanisms in an established model of progeria, we performed RNA-seq on kidney and skeletal muscle from six *Klotho*-KO mice and six age-matched C57BL/6J controls. Klotho is a pro-longevity factor that modulates IGF1–mTOR, NRF2 and TGFβ signalling; its deficiency causes progeria, limiting mouse maximum lifespan to 4–5 months, whereas overexpression extends lifespan[3].

As expected, *Klotho* was highly expressed in control kidneys and was nearly absent in both tissues from *Klotho*-KO mice (Extended Data Fig. 6d). To avoid a direct contribution of *Klotho* expression to tAge predictions, we retrained rodent multi-tissue clocks excluding *Klotho* and applied them to control and *Klotho*-KO samples. Both chronological and mortality clocks detected increased tAge in *Klotho*-KO kidneys and skeletal muscle (Fig. 3f and Extended Data Fig. 6e), with a stronger effect in kidney, where this gene is normally expressed. Among top genes contributing to the pro-mortality shift was *Cdkn1a*, which was upregulated in both tissues of progeroid mice (Fig. 3g), consistent with the role of Klotho in preventing cellular senescence[3]. Overall, gene-level contributions to elevated tAge were positively correlated between kidney and muscle (Pearson's $r = 0.39$; Extended Data Fig. 6f).

Multiple module-specific mortality clocks also showed accelerated tAge in *Klotho*-KO mice, particularly for energy metabolism and NRF2 signalling modules (Fig. 3h and Extended Data Fig. 6g). Clocks trained on genes involved in respiration/mitochondrial translation, oxidative phosphorylation/TCA cycle and cholesterol metabolism/mTOR signalling showed significantly increased tAge in both tissues, whereas NRF2 signalling/proteasome module clocks showed significant and marginally significant tAge acceleration in kidney and muscle, respectively.

Genes from respiration/mitochondrial translation and cholesterol metabolism/mTOR signalling modules were among the strongest contributors to the composite pro-mortality shift in *Klotho*-KO kidneys (Extended Data Fig. 6h). This was accompanied by broad downregulation of genes involved in respiration, mitochondrial translation, oxidative phosphorylation and fatty acid metabolism (Extended Data Fig. 6i and Supplementary Table 7b), mirroring patterns seen in aged and short-lived animals (Fig. 1i) and supporting impaired metabolic function as a key consequence of Klotho deficiency[3]. By contrast, inflammation and interferon modules were downregulated in both tissues of *Klotho*-KO mice and did not contribute to tAge acceleration (Extended Data Fig. 6h,i). Immunity-related module clocks also remained largely unresponsive despite being among the most accurate overall (Fig. 3c), indicating that this progeria model primarily accelerates molecular ageing through metabolic disruption rather than inflammatory activation. Tissue-specific effects were also observed: ECM organization/EMT and muscle contraction/cytoskeleton modules accelerated tAge selectively in kidney and muscle, respectively (Fig. 3h).

To test whether *Klotho*-KO induces a systemic pro-ageing effect across cell types, we performed snRNA-seq of kidney and brain from an 8-week-old control mouse and an age-matched *Klotho*-KO mouse. Uniform manifold approximation and projection (UMAP) resolved major kidney and brain cell types (Fig. 3i,j), and *Klotho* expression was substantially reduced across kidney cell types in *Klotho*-KO mice (Extended Data Fig. 6j), in agreement with the bulk data. After aggregating metacells (around 200K reads per metacell) separately for each cell type and genotype and applying rodent multi-tissue clocks trained excluding *Klotho*, the mortality clock detected significant tAge acceleration in all kidney cell types except loop of Henle (Fig. 3i), whereas the chronological clock showed similar but less uniformly significant effects (Extended Data Fig. 6k). Mortality tAge gene contributions in proximal tubule cells correlated with bulk kidney (Pearson's $r = 0.57$; Extended Data Fig. 6l), highlighting consistency between snRNA-seq and bulk RNA-seq. Top shared pro-mortality kidney biomarkers included upregulated *Cdkn1a* and *Cp* (encoding ceruloplasmin glycoprotein, which is implicated

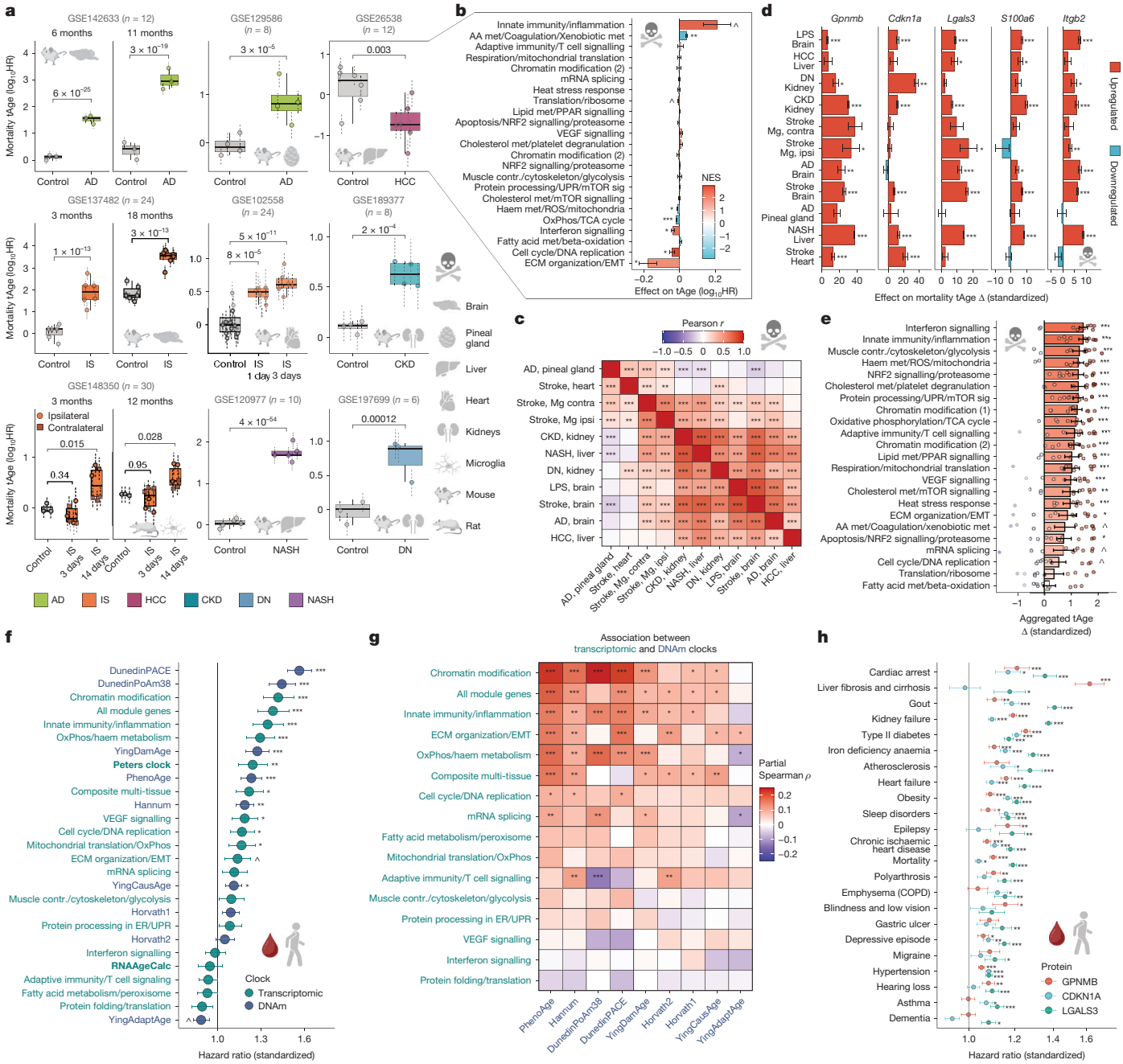

Fig. 5 | See next page for caption.

in iron metabolism and elevated in multiple disease models[44]), and downregulated *Mogat1*, *Cyp51* and *Fmo5*.

In brain, baseline *Klotho* expression in controls was lower, and its knockout-associated downregulation was significant only in neurons and oligodendrocytes, with similar trends in most other cell types except oligodendrocyte precursor cells (Extended Data Fig. 6m). Both mortality and chronological clocks detected significant tAge acceleration in neurons, astrocytes and oligodendrocytes, and marginally significant acceleration in endothelial cells ($P_{adj} \leq 0.079$; Fig. 3j and Extended Data Fig. 6n). By contrast, microglia showed a marginal decrease in mortality tAge ($P_{adj} = 0.076$), consistent with the absence of inflammatory activation in *Klotho*-KO bulk tissues (Fig. 3h and Extended Data Fig. 6i). Together, these results illustrate that a lifespan-regulating intervention can produce contrasting health-associated effects across cell types and functional components, underscoring the heterogeneous nature of ageing and mortality hallmarks.

Cell damage induces mortality biomarkers

To test whether in vivo ageing and mortality signatures are recapitulated in cellular models of damage accumulation, we applied multi-tissue transcriptomic clocks to in vitro datasets of senescence and stress induction. In cultured human primary fibroblasts, both chronological and mortality universal clocks showed a significant linear increase in tAge over time across donors (Fig. 4a and Extended Data Fig. 7a), coinciding with deceleration of population doublings (Extended Data Fig. 7b). Similar tAge elevation accompanied replicative senescence in control WI-38 cells (Fig. 4b and Extended Data Fig. 7c,d). In both models, tAge correlated more closely with time than with doublings or passage

Fig. 5 | Ageing-related diseases in mammals exhibit shared transcriptomic hallmarks of mortality. a, Mortality tAge of control (grey) and age-matched chronically diseased (coloured) animals estimated with the BR rodent multi-tissue mortality clock. *n* per dataset is indicated next to the source ID. Benjamini–Hochberg-adjusted *P* values from mixed-effects models are shown. Data are tAge point estimates ± s.d. AD, Alzheimer's disease; DN, diabetic nephropathy; IS, ischaemic stroke; NASH, nonalcoholic steatohepatitis. **b**, Contributions of modules to mortality tAge differences between control and HCC livers from 2-year-old B6C3F1 mice ($n = 6$ mice per group), estimated using the composite elastic net rodent mortality clock. Values represent partial tAge differences predicted using only the respective module genes; positive and negative values indicate pro-mortality and anti-mortality changes, respectively, in HCC. Statistical significance was tested with ANOVA. Bar colours indicate module-level expression shifts in HCC (NES computed through GSEA). Red indicates upregulation in HCC and blue indicates downregulation in HCC. Data are point estimates ± s.e. **c**, Pairwise Pearson correlations of gene-level mortality-associated expression changes (logFC or slope × clock coefficient) across disease models, based on the elastic net rodent mortality clock. Correlations were computed using the union of the top 500 differentially expressed genes (lowest limma model *P* values) per pair. Contra, contralateral; ipsi, ipsilateral; Mg, microglia. **d**, Top 5 genes contributing to increased mortality tAge across chronic diseases (standardized logFC or slope × clock coefficient), according to the elastic net rodent mortality clock. Genes were ranked based on mixed-effects model estimates. Data are point estimates of gene contributions ± s.e. **e**, Aggregated effects of chronic diseases on standardized mortality tAge across module-specific rodent mortality clocks ($n = 10$ disease models), estimated with mixed-effects models. Data are weighted mean ± s.e.m. **f**, Association of transcriptomic (green) and DNA methylation (DNAm; blue) clocks with time to death in FHS human blood data ($n = 3{,}698$ for RNA-seq; $n = 1{,}790$ for DNA methylation). Transcriptomic models include elastic net universal mortality clocks and published human chronological clocks (Peters clock and RNAAgeCalc (shown in bold)). DNA methylation models include first and second generation clocks that were not trained on FHS participants. Standardized hazard ratios and *P* values were computed using Cox proportional hazards models adjusted for age and sex. Data are hazard ratio point estimates with error bars exp(logHR ± s.e.). ^$P < 0.1$; *$P < 0.05$; **$P < 0.01$; ***$P < 0.001$. **g**, Partial Spearman correlations between DNA methylation (DNAm; columns) and elastic net universal mortality transcriptomic (rows) clocks, adjusted for age and sex. **h**, Association of plasma GPNMB ($n = 50{,}117$), CDKN1A ($n = 51{,}276$) and LGALS3 ($n = 51{,}647$) with human time to death, disease outcomes and risk factors in UK Biobank (UKB). Hazard ratios for standardized protein concentration and Benjamini–Hochberg-adjusted *P* values were computed using Cox proportional hazards models adjusted for age and sex. Data are hazard ratio point estimates with error bars exp(logHR ± s.e.). In box plots, the centre line is the median, box edges delineate IQR and whiskers extend to ±1.5× IQR. All tests were two-sided where applicable. *P* values were Benjamini–Hochberg-adjusted unless noted; asterisks denote Benjamini–Hochberg-adjusted *P* values: ^$P_{adj} < 0.1$; *$P_{adj} < 0.05$; **$P_{adj} < 0.01$; ***$P_{adj} < 0.001$. Icons in **a**–**f**,**h** created in BioRender; Tyshkovskiy, A. https://BioRender.com/hqvg5ka (2026); and Tyshkovskiy, A. https://BioRender.com/vb612zl (2026).

number (Extended Data Fig. 7e), suggesting that tAge signals precede overt phenotypic decline. Mortality-associated expression changes during culturing were concordant between primary fibroblasts and WI-38 cells (Pearson's $r = 0.7$), with *CDKN1A* among the top contributors (Fig. 4c). Notably, hTERT overexpression in WI-38 prevented senescence (Extended Data Fig. 7d) and abolished the increase in tAge (Fig. 4b and Extended Data Fig. 7c), indicating that transcriptomic clocks primarily capture damage-associated changes rather than time per se. Consistently, induced pluripotent stem cells (iPSCs) derived from human primary fibroblasts showed reduced tAge relative to donor cells by both clocks (Fig. 4d and Extended Data Fig. 7f), consistent with prior molecular studies[21,45].

We next tested whether acute damaging interventions accelerate tAge in vitro. In human primary fibroblasts treated with the metabolic stressors oligomycin or 2-deoxyglucose (2-DG), both clocks detected increased tAge relative to donor-matched controls (Fig. 4e and Extended Data Fig. 7g). Mouse and naked mole rat embryonic and skin fibroblasts exposed to 20 Gy γ-irradiation also showed elevated tAge in both species and cell types (Fig. 4f and Extended Data Fig. 7h), supporting the idea that transcriptomic clocks reflect accumulated damage burden in biological systems. By contrast, neither γ-irradiation nor hTERT overexpression altered DNA methylation age in human cells[46], suggesting that DNA methylation and transcriptomic clocks track complementary aspects of ageing, with epigenetic marks reflecting longer-term stochastic changes and gene expression capturing more dynamic functional states.

tAge acceleration after γ-irradiation was evident across multiple rodent mortality module clocks, including chromatin modification, interferon signalling, respiration/mitochondrial translation, cytoskeleton/glycolysis and cholesterol metabolism/mTOR signalling (Fig. 4g), and was accompanied by upregulation of genes involved in interferon, interleukin and TNF signalling, inflammation and apoptosis (Extended Data Fig. 7i and Supplementary Table 7c).

To characterize pathways that contribute to ageing-associated shifts in human cellular models, we defined multi-species co-expression modules shared across four mammalian species. Rodent and primate modules overlapped substantially (Extended Data Fig. 7j), and WGCNA on the combined meta-dataset revealed 15 multi-species modules that were enriched for specific pathways including inflammation, interferon signalling, ECM/EMT and mRNA splicing (Extended Data Fig. 7k and Supplementary Table 6c,d), each showing higher internal correlation than random gene sets (Extended Data Fig. 7l). We then developed 14 non-overlapping module-specific universal chronological and mortality clocks with mean LOFO performance $r > 0.3$ (Fig. 4h and Supplementary Tables 4c and 5c). As with their rodent counterparts, universal mortality module clocks tracked both chronological age and expected maximum lifespan.

Applying universal clocks to reprogramming data revealed reduced tAge in iPSCs for most chronological and mortality clocks (Fig. 4i and Extended Data Fig. 7m), with the strongest rejuvenation signal in the ECM/EMT module, consistent with dedifferentiation and mesenchymal-to-epithelial transition during reprogramming[47]. EMT-associated genes were correspondingly downregulated in iPSCs (Fig. 4i, Extended Data Fig. 7n and Supplementary Table 7d). Conversely, the metabolic stressors oligomycin and 2-DG increased mortality tAge predominantly in metabolic modules, including fatty acid metabolism, oxidative phosphorylation/haem metabolism, cytoskeleton/glycolysis and mitochondrial translation (Fig. 4j), further supporting the ability of module clocks to pinpoint pathways that are most affected by damage-modulating interventions.

Comparing gene-level contributions to mortality tAge changes across models showed that replicative culturing and γ-irradiation produced similar patterns, whereas reprogramming and hTERT overexpression formed an opposing cluster, and oligomycin and 2-DG were intermediate (Extended Data Fig. 7o). Several genes behaved consistently across cellular damage and rejuvenation models (Fig. 4k), including *Cdkn1a*, the stress-response gene *Apod*, and *Eda2r*, an inflammation regulator and robust ageing biomarker at transcriptomic and proteomic levels[48,49]. These genes thus represent candidate universal biomarkers of ageing- and stress-induced damage accumulation across different levels of biological organization.

Mortality hallmarks of chronic diseases

To examine whether chronic pathology induces ageing- and mortality-associated transcriptomic changes, we analysed nine rodent datasets covering models of Alzheimer's disease, chronic kidney disease (CKD), diabetic nephropathy, ischaemic stroke, nonalcoholic steatohepatitis

Fig. 6 | See next page for caption.

and hepatocellular carcinoma (HCC), each with age-matched controls. Rodent multi-tissue chronological and mortality clocks showed significant tAge acceleration in all disease models and organs except HCC (Fig. 5a and Extended Data Fig. 8a). In ischaemic stroke, mortality tAge in heart increased by day 1 and further by day 3, and brain demonstrated an even stronger increase by day 3 in both young and old animals. Microglia showed consistent increases in tAge across clocks by day 14, with higher tAge in the ipsilateral versus contralateral hemisphere ($P_{adj} < 0.046$). These results highlight spatiotemporal and organ-specific heterogeneity in disease-associated molecular ageing dynamics.

By contrast, HCC livers showed lower mortality tAge than age-matched controls (Fig. 5a). Genes contributing to this signal were enriched for cell cycle, dedifferentiation and ECM organization (*Plekhb1*, *Col1a1*, *Col3a1*, *Col4a1*, *Ube2c* and *Cdk1*; Extended Data Fig. 8b). Accordingly, EMT/ECM and cell cycle modules contributed most strongly to the tAge reduction (Fig. 5b and Extended Data Fig. 8c), and the EMT/ECM module clock showed a marginal tAge decrease ($P_{adj} = 0.08–0.1$; Extended Data Fig. 8d). At the same time, inflammatory and amino acid/xenobiotic metabolism modules contributed to increased tAge (Fig. 5b and Extended Data Fig. 8c), accompanied by upregulation of inflammatory, interferon and p53 signalling, and downregulation of respiration, oxidative phosphorylation and fatty acid metabolism (Extended Data Fig. 8e and Supplementary Table 7e). Many module-specific mortality clocks also displayed increased tAge in HCC (Extended Data Fig. 8f). Together, these data indicate that tumours combine youth-like features, such as proliferation, dedifferentiation and ECM remodelling, with pro-ageing hallmarks, including inflammation and metabolic dysregulation[50].

Fig. 6 | HPB and early embryogenesis exhibit anti-ageing gene expression effects. a, Mortality tAge of livers from 3-month-old (left) and 20-month-old (right) C57BL/6J mice after 3 months of isochronic parabiosis or HPB, estimated with the BR rodent multi-tissue mortality clock ($n = 3$ animals per group). Benjamini–Hochberg-adjusted P values from mixed-effects model are labelled. Data are tAge point estimates ± s.d. **b**, Top 25 genes contributing to pro-mortality and anti-mortality transcriptomic shifts in old heterochronic parabionts ($n = 12$) based on the elastic net rodent mortality clock (logFC × clock coefficient). Contributions and Benjamini–Hochberg-adjusted P values were computed with limma model adjusted for attachment status. Data are point estimates of gene contributions ± s.e. Red and blue indicate upregulation and downregulation, respectively, in heterochronic parabionts. **c**, Standardized mortality tAge differences induced by HPB in old livers ($n = 12$) estimated with module-specific rodent mortality clocks. Group differences were tested with ANOVA including attachment status as a covariate. Colour indicates module-level expression shifts (NES computed through GSEA). Data are point estimates ± s.e. **d**, Chronological tAge during C57BL/6J mouse embryogenesis ($n = 33$) estimated with the BR mouse multi-tissue chronological clock. Overall change was tested with mixed-effects ANOVA; phase-specific slopes (up to embryonic day 10 (E10) and after E10) with linear mixed-effects models. Purple line, loess fit; dashed line, developmental ground zero (minimum tAge) point estimate; shaded area, 95% confidence interval. Data are tAge point estimates ± s.d. **e**, Pearson correlation between developmental day and chronological (left) or mortality (right) tAge estimated with module-specific rodent clocks, computed separately for early (≤E10) and late (>E10) phases. **f**, Pairwise Pearson correlations of gene-level mortality-associated expression changes (logFC or slope × clock coefficient) across age-deceleration models, based on the elastic net rodent mortality clock. Correlations were computed using the union of the top 500 differentially expressed genes (lowest P values) per pair. **g**, Top 6 genes contributing most to decreased mortality tAge across early embryogenesis ($n = 15$), caloric restriction ($n = 8$ caloric restriction models) and HPB in old mice ($n = 12$), according to the elastic net rodent mortality clock (standardized logFC or slope × clock coefficient). Genes were ranked based on mixed-effects model estimates. Data are point estimates of gene contributions ± s.e. **h**, Chronological tAge of C57BL/6 mouse embryonic metacells (E6.5–E8.5) estimated with the BR mouse multi-tissue chronological clock ($n = 34$). Slope and P value were tested with a mixed-effects model. Black curve, loess fit; shaded band, 95% confidence interval. Data are tAge point estimates ± s.d. **i**, Slopes of chronological tAge change across cell lineages during E6.5–E8.5 ($n = 34$) from linear mixed-effects models. Data are slope point estimates ± s.e. ExE, extraembryonic; NMP, neuromesodermal progenitor; HEPs, haematoendothelial progenitors. **j**, Chronological tAge trajectories for selected cell lineages during E6.5–E8.5 ($n = 34$). Slope and P values were tested with a mixed-effects model. Black curve, loess fit; shaded band, 95% confidence interval. Data are tAge point estimates ± s.d. **k**, Screenshot of the TACO app interface for estimating and comparing tAge from gene expression data. In box plots, the centre line is the median, box edges delineate IQR and whiskers extend to ±1.5× IQR. All tests were two-sided where applicable. P values were Benjamini–Hochberg-adjusted unless noted; asterisks denote Benjamini–Hochberg-adjusted P values: $^{\wedge}P_{adj} < 0.1$; $^{*}P_{adj} < 0.05$; $^{**}P_{adj} < 0.01$; $^{***}P_{adj} < 0.001$. Icons in **a**–**j** created in BioRender; Tyshkovskiy, A. https://BioRender.com/hqvg5ka (2026).

Gene-level contributions to increased tAge were broadly concordant across disease models (Fig. 5c and Extended Data Fig. 8g). *Gpnmb*, *Cdkn1a* and *Lgals3* showed the most consistent pro-mortality contributions across diseases, being significantly upregulated in at least five models (Fig. 5d). These genes, implicated in immune modulation and chronic pathology[38,51], also contributed to LPS-induced tAge acceleration in mouse brain, consistent with the positive correlation between LPS- and disease-associated signatures (Fig. 5c and Extended Data Fig. 8g).

Rodent module-specific mortality clocks revealed increased tAge in most cellular subsystems across disease models (Fig. 5e and Extended Data Fig. 8f), with the largest and most consistent effects in interferon and inflammatory modules, in line with their broad upregulation across diseases (Extended Data Fig. 8e and Supplementary Table 7e) and the central role of chronic inflammation in age-related pathology[52]. Only Alzheimer's disease in pineal gland and ischaemic stroke in heart lacked an inflammatory module acceleration and clustered separately (Fig. 5c and Extended Data Fig. 8g).

Consistent with rodent data, universal mortality clocks detected significant tAge acceleration in tissues from human patients with Crohn's disease, ulcerative colitis, CKD, heart failure and Alzheimer's disease after adjustment for age and sex (Extended Data Fig. 8h). To further test whether our mortality clocks prospectively predict time to death, we analysed Framingham Heart Study (FHS) blood data. After adjustment for age and sex, all-cause mortality was significantly associated with tAge predicted by universal composite, multi-module and several module-specific mortality clocks (chromatin modification, inflammation/innate immunity and oxidative phosphorylation/haem metabolism) (Fig. 5f). Several multi-tissue transcriptomic clocks performed comparably to second-generation human blood DNA methylation clocks (DunedinPACE[33], YingDamAge[23] and PhenoAge[31]) and outperformed existing human transcriptomic chronological clocks (Peters[24] and RNAAgeCalc[26]), both in the full cohorts ($n = 3{,}698$ for RNA-seq; $n = 1{,}790$ for DNA methylation) and in the shared subset of patients ($n = 996$) (Fig. 5f and Extended Data Fig. 8i). Notably, the accuracy of chronological age and prediction of time to death was largely uncoupled (Extended Data Fig. 8j)—for example, the Horvath2 clock was most accurate for age but not significantly associated with mortality, whereas DunedinPACE and the chromatin-modification transcriptomic clock showed weaker age correlations but strong mortality associations.

Although trained on different modalities, transcriptomic and DNA methylation clock predictions were positively correlated across patients after adjusting for age and sex (Fig. 5g). Among transcriptomic models, the chromatin-modification clock showed the highest correlation with epigenetic clocks, pointing to interplay between these modalities consistent with the mechanistic relationship between DNA methylation and chromatin state[53].

Finally, we tested whether common transcriptomic biomarkers of ageing, mortality and disease, including *GPNMB*, *CDKN1A*, *LGALS3*, *S100A6* and *ITGB2*, were also associated with time to death and cardiovascular outcomes in human blood. Cox proportional hazards models adjusted for age and sex showed their overall positive associations with mortality and incident cardiovascular disease (CVD), stroke and congestive heart failure (CHF), with *LGALS3* and *S100A6* being significant for most outcomes ($P_{adj} < 0.05$) (Extended Data Fig. 8k). In UK Biobank plasma proteomics data from more than 50,000 participants, GPNMB, CDKN1A and LGALS3 protein levels were positively associated with all-cause mortality, a broad spectrum of diseases (including cardiac arrest, heart failure, liver cirrhosis, diabetes, kidney failure, depression and atherosclerosis) and risk factors (including obesity, hypertension and sleep disorders) (Fig. 5h and Supplementary Table 8). Together, these findings highlight *Gpnmb*, *Cdkn1a* and *Lgals3* as conserved biomarkers of mortality and chronic diseases across tissues, species and molecular layers.

Health-promoting effects of parabiosis

To identify transcriptomic signatures of in vivo molecular age deceleration, we analysed liver gene expression from mice subjected to heterochronic parabiosis (HPB)[54], in which old animals share circulation with young partners and show reversal of multiple ageing-associated phenotypes, exhibiting enhanced stem cell function, remyelination, neurogenesis and angiogenesis, and reduced cardiac hypertrophy[55]. Previously, we showed that HPB reduces epigenetic age (eAge) in blood and liver of 20-month-old mice paired with 3-month-old partners, with effects persisting after detachment and accompanied by lifespan

extension[54], whereas young partners show a transient eAge increase that normalizes after recovery[56].

Here we analysed liver transcriptomes from young and old mice subjected to heterochronic or isochronic parabiosis for 3 months and euthanized either immediately ('attached') or 2 months after detachment ('detached'). In old heterochronic parabionts, the rodent multi-tissue mortality clock detected a significant tAge reduction at the attached time point, whereas the chronological clock showed a nonsignificant trend (Fig. 6a and Extended Data Fig. 9a). Two months after detachment, tAge reduction became significant for both clocks. Young heterochronic parabionts showed higher tAge relative to isochronic controls immediately after HPB, but this difference diminished after recovery, paralleling eAge behaviour[56].

The strongest contributor to the HPB-associated tAge reduction in old mice (attached and detached groups pooled) was *Nrep*, which was upregulated upon exposure to young blood (Fig. 6b), consistent with enhanced regenerative potential[57]. Anti-mortality changes also included downregulation of *Cdkn1a* and *Vcam1*, whose inhibition alleviates neuroinflammation and improves learning and memory in aged mice[58].

HPB-induced tAge deceleration in old mice was reflected across most module-specific clocks (Fig. 6c and Extended Data Fig. 9b), indicating a systemic health-promoting effect spanning multiple subsystems. Consistently, old heterochronic parabionts exhibited downregulation of inflammatory, interferon, p53 and apoptotic pathways, and upregulation of oxidative phosphorylation and lipid metabolism (Extended Data Fig. 9c and Supplementary Table 7f), opposing ageing- and mortality-associated pathway signatures (Fig. 1i). In young mice, the transcriptomic effects of HPB were weaker and mixed, combining pro-mortality and anti-mortality features.

Transcriptome reset during embryogenesis

To examine tAge dynamics during mammalian development, we analysed mouse embryogenesis gene expression profiles from zygote to birth. Prior work reported a DNA methylation rejuvenation phase up to embryonic day 4.5 (E4.5) to E10.5 followed by a monotonic increase in eAge[59], consistent with a 'ground zero' model[60]. Using mouse multi-tissue transcriptomic clocks of chronological age and mortality, we observed a similar U-shaped tAge trajectory (Fig. 6d and Extended Data Fig. 9d), with minimum tAge around E10 and a 95% confidence interval spanning E8.5–E15, supporting a systemic rejuvenation phase at the level of gene expression.

Gene contributions to tAge before and after E10 were anti-correlated (Pearson's $r = -0.42$; Extended Data Fig. 9e), implicating largely shared genes with effects in opposing directions during rejuvenation and post-E10 phases. Key contributors included *Cdkn1a* and the inflammatory regulator genes *S100a8*, *S100a9* and *Lgals3*, which were downregulated up to E10 and upregulated thereafter. Early embryogenesis was also accompanied by a genome-wide mRNA downregulation followed by broad upregulation after E10 (Extended Data Fig. 9f). However, recalculating tAge using only genes that were upregulated or downregulated in each phase still yielded a significant decrease up to E10 and an increase thereafter (Extended Data Fig. 9g), indicating that U-shaped tAge dynamics are not driven solely by global transcriptome remodelling.

Genes that were downregulated up to E10 and subsequently upregulated were enriched for immune response and lipid metabolism, whereas genes with the opposite temporal expression pattern were enriched for cell cycle and mRNA splicing (Extended Data Fig. 9h,i). Consistently, inflammatory response, interferon signalling, p53 pathway and fatty acid metabolism were broadly suppressed up to E10 and subsequently activated (Extended Data Fig. 9c and Supplementary Table 7g). Inflammation and interferon modules were also among the top contributors to the rejuvenation signal based on module contributions and module-specific clocks (Fig. 6e and Extended Data Fig. 9j). Most module clocks (for example, respiration/mitochondrial translation, lipid metabolism and heat stress response) showed U-shaped tAge dynamics (Extended Data Fig. 9k), but some (for example, cell cycle) exhibited elevated tAge during early development, indicating mixed pathway-level signals.

Mortality-associated gene expression changes contributing to tAge deceleration were positively correlated across age-deceleration models, including old HPB, caloric restriction and early embryogenesis (Fig. 6f), with particularly high similarity between HPB and caloric restriction (Pearson's $r = 0.5$). Shared rejuvenation-associated signatures included downregulation of *Cdkn1a* and inflammatory factors *Ccl5*, *S100a9* and *Lgals3* (Fig. 6g). Overall, *Cdkn1a* and *Lgals3* emerge among the most consistent molecular markers of mammalian ageing, rejuvenation and mortality across diseases and lifespan-modulating interventions (Extended Data Fig. 10a).

To test whether embryonic rejuvenation is conserved across cell lineages, we analysed scRNA-seq data obtained from embryos at E6.5–E8.5 and reconstructed ancestral trajectories for each E8.5 cell type using an optimal transport approach. Inferred lineages matched established embryonic origins (Extended Data Fig. 10b,c). At the whole-embryo level (all cells per sample pooled into metacells), both chronological and mortality mouse multi-tissue clocks detected a significant tAge decrease from E6.5 to E8.5 (Fig. 6h and Extended Data Fig. 10d), consistent with bulk data. Lineage-weighted metacells showed significant tAge declines over this interval for almost all examined cell types (Fig. 6i,j and Extended Data Fig. 10e,f) across all three germ layers, including mesoderm (for example, endothelium, paraxial and pharyngeal mesoderm), endoderm (for example, gut) and ectoderm (for example, neural crest and spinal cord). By contrast, extraembryonic endoderm showed a marginal increase in tAge ($P_{adj} = 0.06–0.1$), consistent with elevated eAge of extraembryonic tissues at similar stages[28], suggesting that early rejuvenation may be restricted to intraembryonic lineages. Some lineages (for example, cardiomyocytes) showed a U-shaped curve with tAge increasing from about E8 (Fig. 6j), indicating that the precise timing of the ground zero may vary across tissues and modalities.

Resources for tAge analysis

To facilitate application of transcriptomic clocks, we developed the interactive web platform TACO (http://app.gladyshevlab.org/TACO/) (Fig. 6k) and the R package tAge. These resources implement our preprocessing pipeline, support application of organ-specific and multi-tissue transcriptomic clocks of chronological age, normalized age and expected mortality, and enable visualization and group comparisons.

Discussion

We developed multi-species, multi-tissue transcriptomic clocks of chronological age and expected mortality across >11,000 samples from four mammals, addressing the need for interpretable ageing biomarkers that generalize across organs and species, while reflecting health status. Unlike chronological clocks, which captured detrimental states but were relatively insensitive to lifespan-extending interventions, mortality clocks integrated ageing-associated changes with lifespan-modulating effects and robustly distinguished short- and long-lived animal models. In human blood, these clocks predicted time to death with performance comparable to second-generation DNA methylation clocks while retaining functional interpretability through gene- and module-level readouts.

Across in vivo and in vitro settings, transcriptomic clocks captured damage-associated shifts in chronic disease and cellular stress models and revealed convergent mortality-related markers, including *Lgals3* and *Cdkn1a*. Single-cell analyses further indicated that most cell types, including stem cells, undergo similar pro-mortality changes with age. Network decomposition showed that ageing- and mortality-associated signals are distributed across separable pathway

modules that can be selectively accelerated or rejuvenated by distinct perturbations. Together, these results position transcriptomic clocks as outcome-validated, generalizable, and interpretable biomarkers that complement DNA methylation and proteomic ageing models, enabling subsystem-resolved quantification of molecular age across species, tissues, and cell types. Further discussion is provided in the Supplementary Discussion.

Online content

Any methods, additional references, Nature Portfolio reporting summaries, source data, extended data, supplementary information, acknowledgements, peer review information; details of author contributions and competing interests; and statements of data and code availability are available at https://doi.org/10.1038/s41586-026-10542-3.

1. Gladyshev, V. N. Ageing: progressive decline in fitness due to the rising deleteriome adjusted by genetic, environmental, and stochastic processes. *Aging Cell* **15**, 594–602 (2016).
2. Osorio, F. G. et al. Splicing-directed therapy in a new mouse model of human accelerated aging. *Sci. Transl. Med.* **3**, 106ra107 (2011).
3. Prud'homme, G. J., Kurt, M. & Wang, Q. Pathobiology of the Klotho antiaging protein and therapeutic considerations. *Front. Aging* **3**, 931331 (2022).
4. Fontana, L., Partridge, L. & Longo, V. D. Extending healthy life span—from yeast to humans. *Science* **328**, 321–326 (2010).
5. Harrison, D. E. et al. Rapamycin fed late in life extends lifespan in genetically heterogeneous mice. *Nature* **460**, 392–395 (2009).
6. Brown-Borg, H. M., Borg, K. E., Meliska, C. J. & Bartke, A. Dwarf mice and the ageing process. *Nature* **384**, 33 (1996).
7. Strong, R. et al. Longer lifespan in male mice treated with a weakly estrogenic agonist, an antioxidant, an α-glucosidase inhibitor or a Nrf2-inducer. *Aging Cell* **15**, 872–884 (2016).
8. Miller, R. A. et al. Canagliflozin extends life span in genetically heterogeneous male but not female mice. *JCI Insight* **5**, e140019 (2020).
9. Jiang, N. et al. Sex as a major determinant of pro-longevity drug efficacy: a review of two decades of the NIA Interventions Testing Program. *J. Gerontol. A* **80**, glaf138 (2025).
10. de Magalhães, J. P., Curado, J. & Church, G. M. Meta-analysis of age-related gene expression profiles identifies common signatures of aging. *Bioinformatics* **25**, 875–881 (2009).
11. Timmons, J. A. et al. Longevity-related molecular pathways are subject to midlife "switch" in humans. *Aging Cell* **18**, e12970 (2019).
12. Palmer, D., Fabris, F., Doherty, A., Freitas, A. A. & de Magalhães, J. P. Ageing transcriptome meta-analysis reveals similarities and differences between key mammalian tissues. *Aging* **13**, 3313–3341 (2021).
13. Tyshkovskiy, A. et al. Distinct longevity mechanisms across and within species and their association with aging. *Cell* **186**, 2929–2949.e20 (2023).
14. Tikhonov, S., Batin, M., Gladyshev, V. N., Dmitriev, S. E. & Tyshkovskiy, A. AgeMeta: quantitative gene expression database of mammalian aging. *Biochemistry (Moscow)* **89**, 313–321 (2024).
15. Tyshkovskiy, A. et al. Identification and application of gene expression signatures associated with lifespan extension. *Cell Metab.* **30**, 573–593 (2019).
16. Plank, M., Wuttke, D., van Dam, S., Clarke, S. A. & de Magalhães, J. P. A meta-analysis of caloric restriction gene expression profiles to infer common signatures and regulatory mechanisms. *Mol. Biosyst.* **8**, 1339 (2012).
17. Steinbaugh, M. J., Sun, L. Y., Bartke, A. & Miller, R. A. Activation of genes involved in xenobiotic metabolism is a shared signature of mouse models with extended lifespan. *Am. J. Physiol.* **303**, E488–E495 (2012).
18. Fuentealba, M., Fabian, D. K., Dönertaş, H. M., Thornton, J. M. & Partridge, L. Transcriptomic profiling of long- and short-lived mutant mice implicates mitochondrial metabolism in ageing and shows signatures of normal ageing in progeroid mice. *Mech. Ageing Dev.* **194**, 111437 (2021).
19. Horvath, S. DNA methylation age of human tissues and cell types. *Genome Biol.* **14**, R115 (2013).
20. Hannum, G. et al. Genome-wide methylation profiles reveal quantitative views of human aging rates. *Mol. Cell* **49**, 359–367 (2013).
21. Petkovich, D. A. et al. Using DNA methylation profiling to evaluate biological age and longevity interventions. *Cell Metab.* **25**, 954–960.e6 (2017).
22. Meer, M. V., Podolskiy, D. I. & Tyshkovskiy, A. A whole lifespan mouse multi-tissue DNA methylation clock. *eLife* **7**, e40675 (2018).
23. Ying, K. et al. Causality-enriched epigenetic age uncouples damage and adaptation. *Nat. Aging* **4**, 231–246 (2024).
24. Peters, M. J. et al. The transcriptional landscape of age in human peripheral blood. *Nat. Commun.* **6**, 8570 (2015).
25. Mamoshina, P. et al. Machine learning on human muscle transcriptomic data for biomarker discovery and tissue-specific drug target identification. *Front. Genet.* **9**, 242 (2018).
26. Ren, X. & Kuan, P. F. RNAAgeCalc: a multi-tissue transcriptional age calculator. *PLoS ONE* **15**, e0237006 (2020).
27. Oh, H. S.-H. et al. Organ aging signatures in the plasma proteome track health and disease. *Nature* **624**, 164–172 (2023).
28. Trapp, A., Kerepesi, C. & Gladyshev, V. N. Profiling epigenetic age in single cells. *Nat. Aging* **1**, 1189–1201 (2021).
29. Buckley, M. T. et al. Cell-type-specific aging clocks to quantify aging and rejuvenation in neurogenic regions of the brain. *Nat. Aging* **3**, 121–137 (2023).
30. Lu, A. T. et al. Universal DNA methylation age across mammalian tissues. *Nat. Aging* **3**, 1144–1166 (2023).
31. Levine, M. E. et al. An epigenetic biomarker of aging for lifespan and healthspan. *Aging (Albany NY)* **10**, 573–591 (2018).
32. Lu, A. T. et al. DNA methylation GrimAge strongly predicts lifespan and healthspan. *Aging (Albany NY)* **11**, 303–327 (2019).
33. Belsky, D. W. et al. DunedinPACE, a DNA methylation biomarker of the pace of aging. *eLife* **11**, e73420 (2022).
34. Chu, Y. et al. Glutathione peroxidase-1 overexpression reduces oxidative stress, and improves pathology and proteome remodeling in the kidneys of old mice. *Aging Cell* **19**, e13154 (2020).
35. Junnila, R. K., List, E. O., Berryman, D. E., Murrey, J. W. & Kopchick, J. J. The GH/IGF-1 axis in ageing and longevity. *Nat. Rev. Endocrinol.* **9**, 366–376 (2013).
36. Zhu, C., Xiao, H., Jiang, X., Tong, R. & Guan, J. Prognostic biomarker DDOST and its correlation with immune infiltrates in hepatocellular carcinoma. *Front. Genet.* **12**, 819520 (2022).
37. Johnson, A. A. & Stolzing, A. The role of lipid metabolism in aging, lifespan regulation, and age-related disease. *Aging Cell* **18**, e13048 (2019).
38. Saade, M., Araujo de Souza, G., Scavone, C. & Kinoshita, P. F. The role of GPNMB in inflammation. *Front. Immunol.* **12**, 674739 (2021).
39. Wang, Y. T. et al. Cystatin F–a key player in central nervous system disease. *J. Neuroinflammation* **22**, 203 (2025).
40. Kumari, R. & Jat, P. Mechanisms of cellular senescence: cell cycle arrest and senescence associated secretory phenotype. *Front. Cell Dev. Biol.* **9**, 645593 (2021).
41. Lopez-Otin, C., Blasco, M. A., Partridge, L., Serrano, M. & Kroemer, G. The hallmarks of aging. *Cell* **153**, 1194–1217 (2013).
42. Qin, L. et al. Systemic LPS causes chronic neuroinflammation and progressive neurodegeneration. *Glia* **55**, 453–462 (2007).
43. Vratari, M. & Clayton, Z. Late-onset calorie restriction improves lipid metabolism and aggravates inflammation in the liver of old Wistar rats. *Front. Nutr.* **9**, 899255 (2022).
44. Vassiliev, V., Harris, Z. L. & Zatta, P. Ceruloplasmin in neurodegenerative diseases. *Brain Res. Rev.* **49**, 633–640 (2005).
45. Olova, N., Simpson, D. J., Marioni, R. E. & Chandra, T. Partial reprogramming induces a steady decline in epigenetic age before loss of somatic identity. *Aging Cell* **18**, e12877 (2019).
46. Kabacik, S. et al. The relationship between epigenetic age and the hallmarks of ageing in human cells. *Nat. Aging* **2**, 484–493 (2022).
47. Esteban, M. A. et al. The mesenchymal-to-epithelial transition in somatic cell reprogramming. *Curr. Opin. Genet. Dev.* **22**, 423–428 (2012).
48. Vladimirova, A., Goeminne, L. J. E., Tyshkovskiy, A. & Gladyshev, V. N. A compact protein panel for organ-specific age and chronic disease prediction. Preprint at *bioRxiv* https://doi.org/10.1101/2024.12.09.627624 (2024).
49. Barbera, M. C. et al. Increased ectodysplasin-A2-receptor EDA2R is a ubiquitous hallmark of aging and mediates parainflammatory responses. *Nat. Commun.* **16**, 1898 (2025).
50. Hanahan, D. & Weinberg, R. A. Hallmarks of cancer: the next generation. *Cell* **144**, 646–674 (2011).
51. Shen, Y. et al. Galectin-3 modulates microglial activation and neuroinflammation in early brain injury after subarachnoid hemorrhage. *Exp. Neurol.* **377**, 114777 (2024).
52. Lopez-Otin, C., Blasco, M. A., Partridge, L., Serrano, M. & Kroemer, G. Hallmarks of aging: an expanding universe. *Cell* **186**, 243–278 (2023).
53. Li, Y., Chen, X. & Lu, C. The interplay between DNA and histone methylation: molecular mechanisms and disease implications. *EMBO Rep.* **22**, e51803 (2021).
54. Zhang, B. et al. Multi-omic rejuvenation and lifespan extension on exposure to youthful circulation. *Nat. Aging* **3**, 948–964 (2023).
55. Lagunas-Rangel, F. A. Aging insights from heterochronic parabiosis models. *npj Aging* **10**, 38 (2024).
56. Poganik, J. R. et al. Biological age is increased by stress and restored upon recovery. *Cell Metab.* **35**, 807–820.e5 (2023).
57. Conboy, I. M. et al. Rejuvenation of aged progenitor cells by exposure to a young systemic environment. *Nature* **433**, 760–764 (2005).
58. Yousef, H. et al. Aged blood impairs hippocampal neural precursor activity and activates microglia via brain endothelial cell VCAM1. *Nat. Med.* **25**, 988–1000 (2019).
59. Kerepesi, C., Zhang, B., Lee, S.-G., Trapp, A. & Gladyshev, V. N. Epigenetic clocks reveal a rejuvenation event during embryogenesis followed by aging. *Sci. Adv.* **7**, eabg6082 (2021).
60. Gladyshev, V. N. The ground zero of organismal life and aging. *Trends Mol. Med.* **27**, 11–19 (2021).

[1]Division of Genetics, Department of Medicine, Brigham and Women's Hospital, Harvard Medical School, Boston, MA, USA. [2]Belozersky Institute of Physico-Chemical Biology, Moscow State University, Moscow, Russia. [3]Faculty of Bioengineering and Bioinformatics, Moscow State University, Moscow, Russia. [4]Institute of Molecular Health Sciences, Department of Biology, ETH Zürich, Zurich, Switzerland. [5]Department of Neurology and Neurosurgery, McGill University, Montreal, Quebec, Canada. [6]Metabolic Disorders and Complications Program, Research Institute of the McGill University Health Centre, Montreal, Quebec, Canada. [7]Brain Repair and Integrative Neuroscience Program, Research Institute of the McGill University Health Centre, Montreal, Quebec, Canada. [8]Tohoku University School of Medicine, Sendai, Japan. [9]Department of Clinical Biology and Hormonal Regulation, Tohoku University Graduate School of Medicine, Sendai, Japan. [10]Department of Nephrology, Tohoku University Graduate School of Medicine, Sendai, Japan. [11]Faculty of Engineering Sciences, Heidelberg University, Heidelberg, Germany. [12]T. H. Chan School of Public Health, Harvard University, Boston, MA, USA. [13]Massachusetts College of Pharmacy and Health Sciences, Boston, MA, USA. [14]Department of Genetics, School of Medicine, Stanford University, Stanford, CA, USA. [15]Division of Experimental Medicine, Department of Medicine, McGill University, Montreal, Quebec, Canada. [16]The Jackson Laboratory, Bar Harbor, ME, USA. [17]Geriatric Research, Education and Clinical Center and Research Service, South Texas Veterans Health Care System, Department of Pharmacology, Barshop Institute for Longevity and Aging Studies at The University of Texas Health Science Center at San Antonio, San Antonio, TX, USA. [18]Division of Medical Science, Tohoku University Graduate School of Biomedical Engineering, Sendai, Japan. [19]Broad Institute of Harvard and MIT, Cambridge, MA, USA. ✉e-mail: atyshkovskii@bwh.harvard.edu; vgladyshev@bwh.harvard.edu